# A polychromatic pyramid wavefront sensor with MKID technology for extreme adaptive optics

Aurélie Magniez, Lisa Bardou, Charlotte Z. Bond, David Barr, Marta Escriche, Deli Geng, Timothy J. Morris, Kieran O'Brien, Noah Schwartz, Pieter J. de Visser

**Published version information:**

**Citation:** Aurélie Magniez et al., A polychromatic pyramid wavefront sensor with MKID technology for extreme adaptive optics, Proceedings Volume 13097, Adaptive Optics Systems IX; 130971U (2024)

**DOI:** https://doi.org/10.1117/12.3020052

# A polychromatic pyramid wavefront sensor with MKID Technology for extreme adaptive optics

Aurélie Magniez[a], Lisa Bardou[a], Charlotte Z. Bond[b], David Barr[a], Marta Escriche[a], Deli Geng[a], Timothy J. Morris[a], Kieran O'Brien[a], Noah Schwartz[b], and Pieter J. de Visser[c]

[a]Durham University, Department of Physics, South Road, Durham, DH1 3LE, UK
[b]UK Astronomy Technology Centre, Royal Observatory, Edinburgh EH9 3HJ, UK
[c]SRON Netherlands Institute for Space Research, Niels Bohrweg 4, Leiden 2333 CA, Netherlands

## ABSTRACT

The next generation of adaptive optics (AO) systems have chosen the pyramid wavefront sensor (PWFS) that is renowned for its performance in closed-loop AO. With the advent of the extremely large telescope era, it is essential to investigate methods to enhance PWFS performance further. Microwave Kinetic Inductance Detectors (MKID) are photon-counting devices that record the arrival time and energy of each incident photon. They offer new capabilities beyond those of existing detectors and can significantly improve AO performance. This project aims to demonstrate how the use of an MKID can improve PWFS performance to meet the demanding requirements of an ELT instrument through simulation, laboratory tests and finally an on-sky demonstration. Here we introduce the project, presenting preliminary simulation results and detailing the optical bench.

**Keywords:** Pyramid WFS, Polychromatic wavefront sensing, MKID, eXtreme Adaptive Optics

## 1. INTRODUCTION

Developed for astronomy in 1953,[1] Adaptive Optics (AO) is a key technology that significantly improves the observation abilities of ground-based telescopes. As we move towards the era of Extremely Large Telescopes (ELTs), new challenges emerge, particularly for high-contrast observations. Future high contrast instruments, such as the ELT's Planetary Spectrograph Camera (PCS),[2] will require unprecedented angular resolution, calling for large scale extreme AO systems (XAO) and improvements in wavefront sensing. The pyramid wavefront sensor (PWFS)[3] achieves high sensitivity and is the WFS of choice for future XAO systems. A crucial element of the PWFS is its detector. While existing technologies satisfy the resolution requirements for PCS, research into alternatives continues. This raises an engaging question: can performance be enhanced by integrating advanced detector technology that provides more information?

In this context, we propose the use of a Microwave Kinetic Inductance Detectors (MKID) array[4] to improve the performance of a PWFS. An MKID brings additional chromatic and temporal information, extending the capabilities provided by traditional semiconductor detectors. Although MKID technology is still in development, it holds significant promise. Whilst the energy sensitivity of the detector can enable the use of multiple bands simultaneously, increasing the number of photons for the wavefront measurement, the additional temporal and chromatic information can be used to address other errors in the wavefront measurement. Initially, we have considered the potential benefits of energy (wavelength) resolution.

The first section of this article presents the concept and the principle of operation of such a system, outlining some of the potential benefits. Then the simulation is presented, with two principal objectives: first, it aims to explore how integrating MKID technology can enhance the performance of a PWFS; second, it seeks to define the specific requirements for an effective MKID array. Finally, the bench demonstration is presented and will provide a practical proof of concept by implementing an MKID-based PWFS. We discuss the optical bench layout, the anticipated performance of the MKID device, and the entire process from device readout to real-time control (RTC). Through this demonstration, we aim to validate our concept and outline the significant improvements it can bring to high-contrast astronomical applications.

Adaptive Optics Systems IX, edited by Kathryn J. Jackson, Dirk Schmidt, Elise Vernet,
Proc. of SPIE Vol. 13097, 130971U · © 2024 SPIE · 0277-786X
doi: 10.1117/12.3020052

## 2. CONCEPT

By using an MKID as the WFS detector, we have a measure of the energy of the photon. It then becomes possible to sort them into wavebands. The number of wavebands as well as their central wavelengths is dependent on the energy resolution of the device. We can then run the system like a multi-PWFS system in which every WFS would operate at different wavelengths simultaneously sensing the same wavefront.

From there, it becomes possible to mitigate the chromatic dispersion of the prism and increase the number of detected photons for the same magnitude star.[5] This is also made possible by the large sensing range of an MKID.[6] This increase in photon flux allows to observe fainter stars. But also, to take advantages to the use of both sensing in the IR and visible. This approach allows us to exploit the characteristics of the two ends of the sensed spectrum.

In this section, we first look at the difference in the performance of the PWFS in the visible and infrared by doing a noise analysis and looking at the optimum performance. We then look at a specific example of how to use the chromatic information to mitigate the non-linearities of the PWFS.

### 2.1 Performance versus wavelength

The choice of the waveband for an AO system depends on multiple factors: the wavebands required by the science observations, the available detector technology, and optical design constraints, to name a few. In terms of AO performance, there is often a trade-off between the linear range of a sensor and the sensitivity of the measurements.[7] Considering a PWFS at the diffraction limit, shorter wavelengths produce higher SNR signals, as the phase to be measured is larger and therefore the signal on the PWFS is stronger. Longer wavelengths have a reduced SNR but larger linear range, with less susceptibility to non-linear effects (optical gains closer to 1). For a classical PWFS working at a single waveband, the choice of waveband is a balance between linear range and sensitivity. The width of the band also involves some trade-offs. A wider band will collect more photons but without knowledge of the exact wavelength distribution, the reconstruction accuracy is impaired. Additionally, a wider band puts additional constraints on the WFS optics - in the case of a PWFS, this requires tighter achromatic constraints to avoid smearing the PWFS pupil images. The use of a polychromatic PWFS with knowledge of the wavelength of incident photons would enable operation across a much larger range of wavelengths, allowing the collection of more photons and the ability to combine the benefits of shorter and longer wavelengths.

Further consideration of the sensitivity of the PWFS measurements shows that the diffraction limit analysis is only valid during the best-seeing conditions. In reality, the system will operate using an AO-corrected PSF where optical gains play an important part in the response of the PWFS, particularly for short wavelengths. We therefore need to consider the impact of optical gain on the sensitivity of the PWFS. Considering only photon noise the noise variance for an open loop PWFS measurement of phase $\phi_i$ is given by:[8]

$$\sigma^2(\phi_i) = \frac{1}{s_{pn}^2(\phi_i) \times N_{photons}} \tag{1}$$

where $N_{photons}$ is the total number of photons per frame and $S_{pn}(\phi_i)$ is the sensitivity with respect to photon noise:

$$S_{pn}(\phi_i) = \left|\left| \frac{\delta I(\phi_i)}{\sqrt{I_0}} \right|\right|_2 \tag{2}$$

where $\delta I(\phi_i)$ is the normalised response of the PWFS to $\phi_i$ and $I_0$ is the normalised reference signal (typically the signal for a flat wavefront). If we consider the noise propagation for each of the control modes of the system $\delta I(\phi_i)$ becomes the elements of the interaction matrix (IM). To incorporate the optical gain effect each element in the IM is simply multiplied by the optical gain for that mode, assuming an IM measured using a diffraction-limited PSF.

Using equations 1 and 2 the expected photon noise variance was computed for different wavelengths, using the PWFS convolutional model[9] to compute the optical gains due to AO fitting errors for different seeing conditions (a range of Fried parameter, $r_0$). The system parameters used in these computations are detailed in Table 1. The results are summarised in Figure 1. The photon noise in terms of wavefront RMS for a single open loop

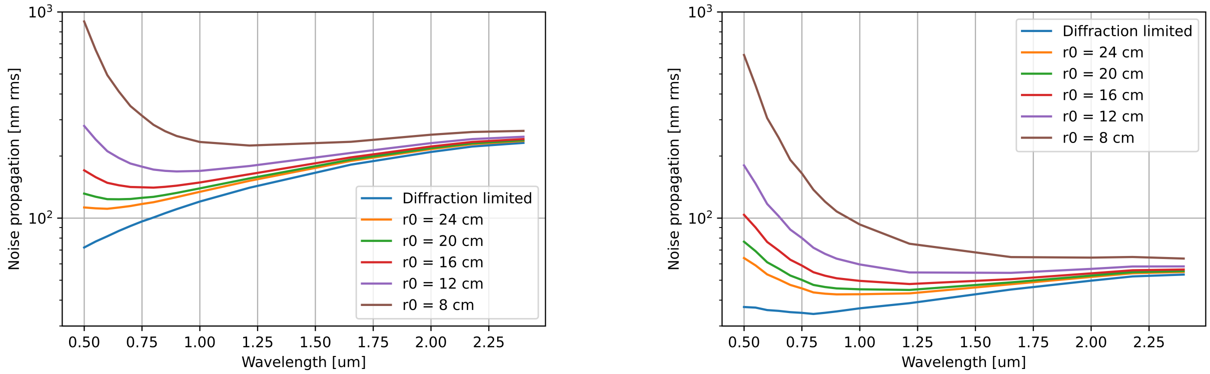


(a) Total photon noise (300 modes)

(b) Low order (first 20 modes) photon noise

Figure 1: Photon noise vs. wavelength for different seeing conditions

PWFS measurement is shown for all the controlled modes in Figure 1a and for the lower order modes only in Figure 1b.

In the case of the total photon noise (1a), the noise behaves as expected for the diffraction-limited case - the shortest wavelengths exhibit the least noise (highest SNR) whilst the noise is the greatest for the longest wavelengths. However, as the seeing degrades (smaller $r_0$) and the residual errors increase we observe that the noise begins to increase, with a greater increase at shorter wavelengths. This is due to the wavefront residuals which effectively broaden the PSF and modify the PWFS signals in a similar way to modulation, leading to a decrease in sensitivity. As the residual wavefront has a much larger impact at shorter wavelengths, the decrease in sensitivity - and hence the increase in noise - is greater. For worse seeing, the effect is greater, resulting in a wavelength-dependent noise minima occurring at longer wavelengths as the observing conditions deteriorate.

The noise varies depending on spatial mode. If we consider only the lower orders (1b) we observe that the minimum noise for these modes occurs at a longer wavelength than for all 300 modes. The optimal wavelength for a PWFS, in terms of minimising photon noise, therefore not only varies with the residual wavefront error (i.e. with seeing conditions) but varies by mode. The use of a polychromatic PWFS would potentially enable optimal weighting of the measurements at different wavelengths, minimising the noise propagation for each mode and extending the performance of the sensor. Such optimisation depends on the number of photons per band and a measurement of the optical gain, both of which are possible with an energy-sensitive photon counting detector such as an MKID.

## 2.2 Optical gain tracking

The PWFS experiences non-linearities due to differences in response between calibration and observation conditions. These non-linearities manifest as a loss in sensitivity that varies with spatial frequency, known as optical gains. We define $c_{true}(\phi_i)$ as the true coefficient value of mode $\phi_i$ in the incoming wavefront while $c(\lambda, \phi_i)$ and $g_{opt}(\lambda, \phi_i)$ are respectively the coefficient and the optical gain values for mode $\phi_i$ for the WFS measurement at wavelength $\lambda$. Then:

$$c(\lambda, \phi_i) = g_{opt}(\lambda, \phi_i) \times c_{true}(\phi_i). \tag{3}$$

There are several techniques to measure optical gains,[9,10] which require an understanding of the behaviour of the loop under varying atmospheric conditions. In a polychromatic WFS system such as the one presented here, it becomes possible to compare the different chromatic wavefront reconstructions simultaneously to monitor the variations of the optical gains. Using equation 3, we define $R_{og}(\phi_i)$ the vector of the ratios of the optical gains at 2 different wavelengths that is equal to the ratios of the modal reconstructions of wavefront:

$$R_{og}(\lambda, \phi_i) = \frac{g_{opt}(\lambda, \phi_i)}{g_{opt}(\lambda_0, \phi_i)} = \frac{c(\lambda, \phi_i)}{c(\lambda_0, \phi_i)}, \tag{4}$$

where $c(\lambda_0, \phi_i)$ and $g_{opt}(\lambda_0, \phi_i)$ are respectively the coefficient modal reconstruction of the wavefront vector and the optical gain vector for the measurement by the WFS at a given reference wavelength $\lambda_0$. We chose to define $\lambda_0$ as the longest central wavelength of the different wavebands sorted by the MKID array as it has the greatest linear range and optical closest to 1, keeping the expected reconstruction ratios between 0 and 1.

Figure 2 represents the chromatic variation of optical gains for different atmospheric conditions for different spatial modes. The gains have been computed using the convolutional model. From the figure, we can observe that the optical gain varies with wavelength and with the observing conditions ($r_0$). From there, it becomes possible to build a model to track the optical gain and by extension the atmospheric conditions, directly using the chromatic modal reconstructions of the MKID-based PWFS.

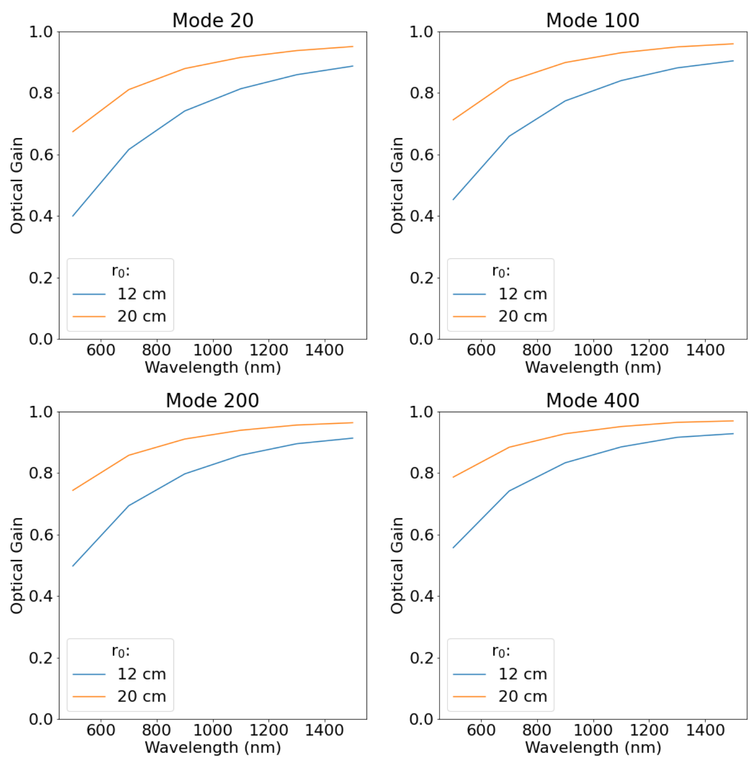


Figure 2: Chromatic variation of optical gain using the convolutional model[9] at different $r_0$ values.

### 2.3 Microwave kinetic inductance detectors (MKID)

MKIDs are superconductor detectors which can provide additional information about incident photons compared to traditional semiconductor detectors - specifically their energy and time of arrival. An incident photon is detected using a probe signal. We then measure the phase of that signal. When a photon hits the sensitive part of the detector a pulse is induced in the phase signal. As the height of the pulse is related to the energy of the photon, we also have access to a measure of the wavelength. The advantage of the MKID over superconductor detectors such as the TES, is that they can be more easily multiplexed into arrays.[11,12] The output of the devices is then a list of photons for which is provided a position, a measure of the energy and an arrival time.

The MKID pulse-response typically shows an exponential decay. If another photon hits the sensitive part of the MKID before the phase stream is back to its stable state, the pulses stack and the measure of the energy is complex as there is non-linearity involved in this multiple event. This leads to saturation effects for high photon flux. It is possible to tune the pulse decay constant when manufacturing the device, mainly by the choice of material. However, shortening the pulse will result in a decrease in energy resolution. The determination of the maximum of the decay constant will be determined by the minimum number of photons required per pixel per second.

Once the list of photons is generated, the Real Time Controller (RTC) can then reconstruct a series of frames for each defined waveband and proceed to the reconstruction of the wavefront. The photon counting capacity of an MKID array allows for further temporal flexibility, such as varying frame rates to uniform the signal-to-noise ratio at each AO loop iteration. However, as a first demonstration of the system, we will focus on the chromatic aspects. The system studied here is considered as a series of PWFS operating at different wavebands, with a constant frame rate identical across all the measurements.

## 3. SIMULATION

Modelling a polychromatic PWFS is essential for understanding the system and probing the potential benefits of polychromatic wavefront sensing. It is also crucial for defining the requirements of the MKID devices needed for different AO systems. In this section we describe the AO simulation, including the implementation of a polychromatic optical gain tracking algorithm, and present preliminary results.

### 3.1 Polychromatic PWFS simulation

A single conjugate AO PWFS system for an 10 m telescope is modelled using the Object-Oriented Python AO package (OOPAO[13]). The simulation parameters are summarised in table 1. In order to simulate a polychromatic sensor a natural guide star (NGS) object and PWFS object are used for each specified waveband. Currently, each band is defined as a single wavelength. The modulation in radians is the same for each wavelength, corresponding to different multiples of $\frac{\lambda}{D}$. The wavefront can be measured at each defined wavelength individually (single-band case) or by combining simultaneous measurements made at different wavelengths (polychromatic case). When using multiple wavelengths, the modulation in $\frac{\lambda}{D}$ is given for the first specified wavelength (typically the shortest).

For the polychromatic case, the measurements at each wavelength can be combined in different ways. The polychromatic reconstructor can be optimised by weighting measurements taken at different wavelengths according to the estimated noise propagated through the reconstruction process for each individual wavelength (see section 2.1). These weightings will depend on the response of the PWFS at the specific wavelength, the optical gain (dependent on observing conditions), and the number of photons in the specific waveband. This optimisation of the polychromatic reconstructor is currently under investigation. In the results presented here, the polychromatic case concatenates the WFS signals from multiple wavebands into a single vector of WFS measurements. A corresponding command matrix is built from this combined response to each spatial mode and used to compute the polychromatic reconstruction.

| Parameter | Value |
|---|---|
| Telescope diameter | 10 m |
| Simulation resolution | $80 \times 80$ |
| PWFS sampling | $20 \times 20$ |
| Modulation | $3\frac{\lambda}{D}$ |
| No. controlled modes | 300 |
| Frame rate | 1 kHz |
| Delay | 2 frames |
| Average wind speed | 11 m/s |
| $r_0$ | 16 cm |

Table 1: Default simulation parameters

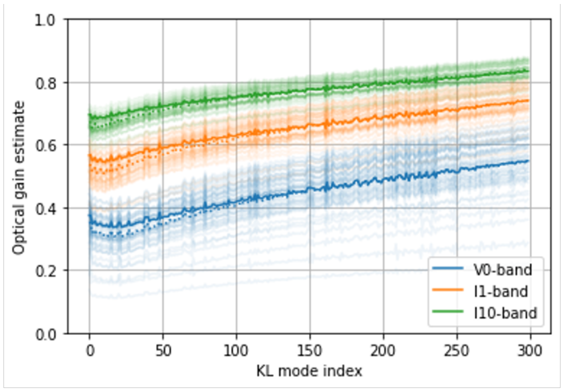


(a) Optical gains for individual closed loop PSFs (faint lines) and an average of the optical gains (dark lines).

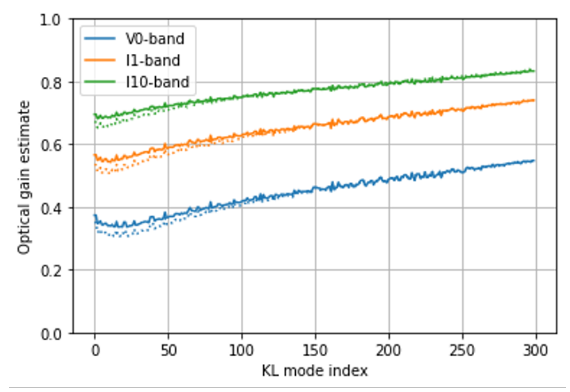


(b) Optical gains using a model fitting error PSF (dark lines) and an average of the optical gains for individual closed-loop PSFs (dashed lines).

Figure 3: Closed loop optical gains computed using the convolutional model for different wavelengths (V0 = 500 nm, I1 = 700 nm, I10 = 900 nm) and for $r_0 = 16$ cm. The loop is closed using a PWFS working at 900 nm.

### 3.2 Polychromatic optical gain tracking

As discussed in section 2.2, the optical gain effect is wavelength dependent - shorter wavelengths suffer a larger reduction in optical gain due to AO residuals. Using a polychromatic PWFS, the ratio of the optical gain for each mode at each wavelength can be estimated as the ratio of the wavefront reconstructions at each wavelength. In the first instance, the optical gain can be tracked with respect to the longest wavelength, the wavelength with optical gains closest to 1. In this case, the optical gain estimates at all other wavelengths are updated by taking a temporal average of the reconstruction ratios. The optical gain estimate is then used to compensate the reconstructed modes at each wavelength:

$$c_{comp}(\lambda, \phi_i) = \frac{1}{g_{opt}(\lambda, \phi_i)} c_0(\lambda, \phi_i) \tag{5}$$

where $c_0$ are the original reconstructed modal coefficients and $g_{opt}$ are the estimated optical gains.

In order to compute the true optical gain, we require an optical gain model to fit the reconstruction ratios and return an estimate of the optical gain for all wavelengths. We use the convolutional model.[9] To compute the response of the PWFS, the model requires an estimate of the PSF on the tip of the pyramid. For the calibration case, this is the modulated diffraction-limited PSF. To compute the closed loop response, and the optical gain, an estimate of the closed loop PSF is required. In our model, we compute the closed-loop PSF from a model of the residual phase PSD. To simplify the computation, we have assumed the majority of the wavefront residual is due to the AO fitting error. The PSF estimate therefore requires only an estimate of the fitting error, computed from the number of AO control modes and a value for $r_0$. Comparisons of the optical gains computed using the fitting-only model and using the true closed loop PSFs are shown in figure 3. The closed loop PSFs were generated from end-to-end simulations, for a high flux case, and the simulation parameters are outlined in table 1. In 3a, the optical gain for short exposure PSFs corresponding to different iterations of the closed loop are plotted. The average of these gains conforms well to the fitting-only model, as shown in 3b, supporting the use of the model to track the average optical gains in cases where the fitting error is the dominant source of error (e.g. in the high flux regime). The optical gains at each iteration of the loop are spread around the average, with a wider spread for shorter wavelengths.

The convolutional model can now be used to compute a set of reference optical gain ratios per mode for each wavelength with respect to a reference wavelength (typically the longest wavelength). This is done for a range of values of $r_0$ - the results presented here use a range of 6 cm to 25 cm in 1 cm increments. The temporally averaged reconstruction ratios are fitted to the optical gain ratios computed using the model - returning a value for $r_0$ and the optical gain values which most closely align with the closed loop reconstruction ratios. Figure 4

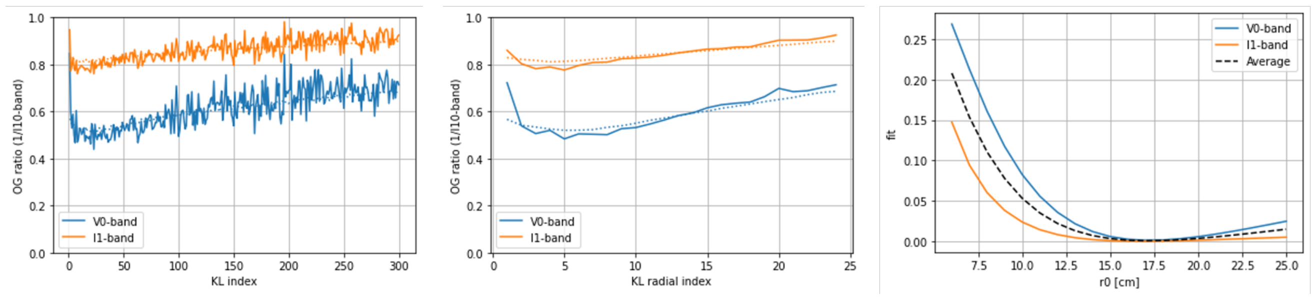


(a) Temporally averaged closed loop reconstruction ratios (solid lines) and fitted model (dashed lines).

(b) Temporally and radial index averaged reconstruction ratios (solid lines) and fitted model (dashed lines).

(c) Fit between closed-loop data and optical gain model parameterized by $r_0$.

Figure 4: Plots representing different stages of the chromatic optical gain tracking algorithm applied to a closed loop simulation. 3 different wavelengths (V0 = 500 nm, I1 = 700 nm, I10 = 900 nm) are used, with the longest wavelength (I10) used as the reference measurement. The loop is simulated for $r_0 = 16$ cm and the closed loop data is averaged over 5 s (5000 loop iterations).

shows some examples of the fitting process. In 4a the closed loop reconstruction ratios averaged over 5000 loop iterations (5 s) are plotted for each spatial mode. In 4b the same data is plotted but averaged over each radial index of the KL mode, to further average out noise in the data. The optical gains per radial index are then compared with the model set using a least squares approach. The result of the fit is shown in 4c. In this example, the algorithm returned an estimate of $r_0$ of 17 cm, close to the true value of 16 cm. The model optical gain ratios corresponding to the fit are plotted for comparison with the closed loop data in 4a and 4b, demonstrating good agreement. Using the radial index averaging approach provides a good estimate of $r_0$ with less data, achieving the same results with only 100 loop iterations (0.1 s).

Future work will further develop the optical gain model, incorporating additional errors for a more accurate fit. This is particularly required for cases where the optical gain is not well described by the impact of the fitting error only, such as low flux/ high noise cases.

### 3.3 Preliminary results

In figure 5, some preliminary simulation results are shown, demonstrating the performance of a polychromatic PWFS using 3 and 5 bands compared to different single waveband cases. Each polychromatic case covers a range of wavelengths between R-band (640 nm) and H-band (1650 nm). In these preliminary results, an equal number of photons per band is used and only photon noise is included. The results shown here include the compensation for optical gains using the fitting error model outlined above, as well as an optimisation of the modal loop gains.

In figure 5a, the K-band Strehl ratio is used as the performance metric versus the number of photons per waveband. We observe that the performance of the polychromatic PWFS is extended to a smaller number of photons per waveband, demonstrating an effective improvement in limiting magnitude. This is primarily driven by the additional number of photons collected across the multiple wavebands. The performance of the single wavebands demonstrates that the longer wavelength PWFS (H-band) performs best, as the larger optical gain effects for the shorter wavelength case (R-band) not only decrease the accuracy of reconstruction but also decrease the SNR, resulting in a significant drop in performance for a smaller number of photons. On the other hand, for the polychromatic PWFS, the combination of measurements at multiple wavelengths and optical gain compensation allows the system to benefit from the additional photons, whilst limiting the impact of the significant optical gain effect at shorter wavelengths.

Figure 5b shows a radial average of the Power Spectral Density (PSD) of the closed loop wavefront for the different cases for high flux conditions, representative of the contrast. The polychromatic PWFS provides a 2 - 3 factor improvement in residual wavefront within the correction band compared to the H-band case.

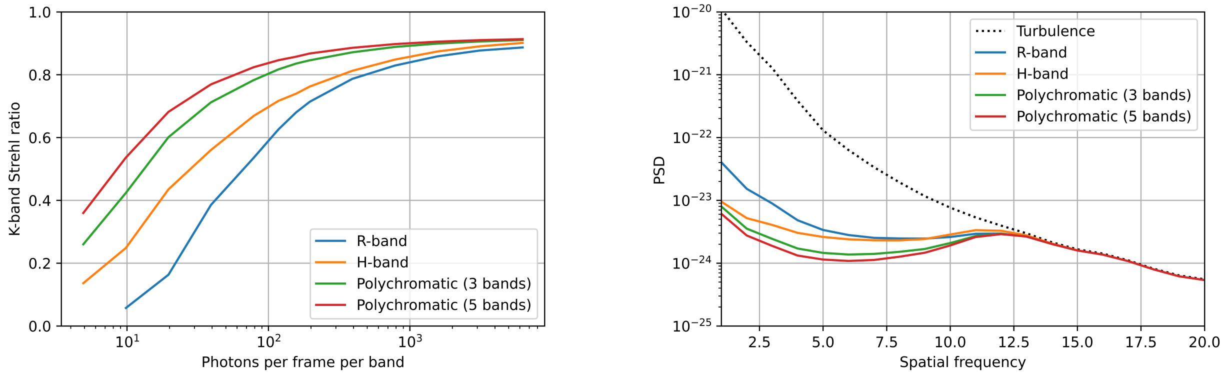


(a) K-band Strehl ratio (b) PSD of the closed loop wavefront

Figure 5: Simulated closed loop performance for single band and polychromatic PWFS AO systems.

# 4. DEMONSTRATION

To test the capabilities of the MKID as a detector suitable for a PWFS we are developing an laboratory AO bench. The design follows a SCAO set-up that will allow the 4-pupil output of a single pyramid prism to illuminate two independent detectors instead of one. One of the detectors is an MKID array, the other a CMOS camera (First Light Imaging C-Blue[14]) on which the pyramid output is imaged four times at different wavelengths. There are several goals behind this two-detector setup. In the first phase of the experiment, the polychromatic set-up on the CMOS camera will allow progressive implementation of multi-wavelength control of the AO loop with a detector whose behaviour is well known. Later, the CMOS camera will act as a control to compare the measurements made with the MKID. Once the MKID measurements are well understood and can be used to effectively control the AO loop, we will be able to compare performance between the CMOS camera and the MKID array.

In this section, we first describe the layout of the bench and the characteristics of the AO system it reproduces before detailing the properties of the MKID array which will be used in the development led on the read-out system, and the integration with the RTC. Finally, we discuss the steps we plan to take in the development of the experiment.

## 4.1 Bench and optical design

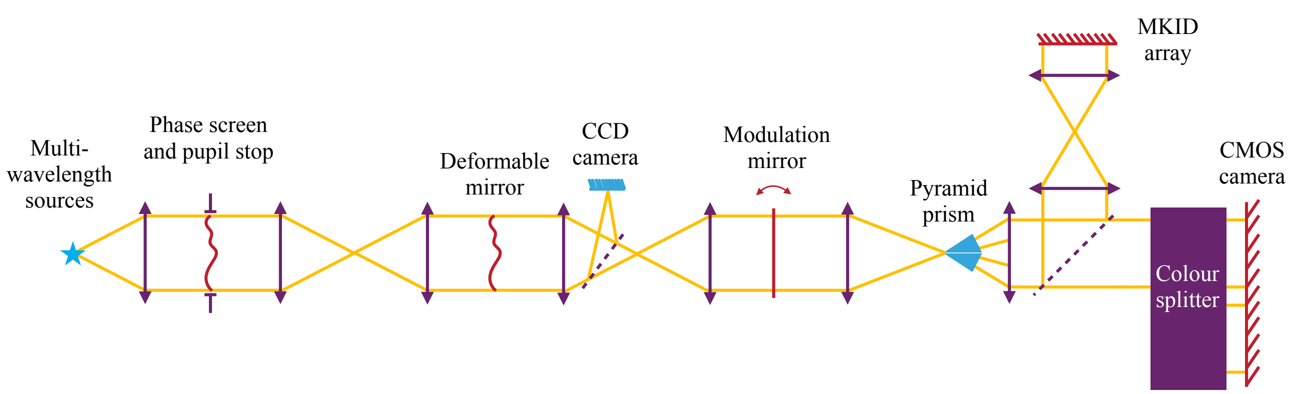


Figure 6: Schematic drawing of the bench design. Focal planes are represented in blue and pupil planes in red.

A schematic diagram of the layout of the bench is shown in Figure 6. There are three optical relays in between the bench sources and the pyramid prism. The focusing elements are made with a stock parabolic mirror of which only a portion is used to make an off-axis parabola for achromatic performance across the wide wavelength range made possible by the MKID. The first relay images an 20 mm diameter pupil on transparent phase screens. The second relay places an 26.5 mm diameter pupil at the location of the deformable mirror (DM) - a 292-actuator

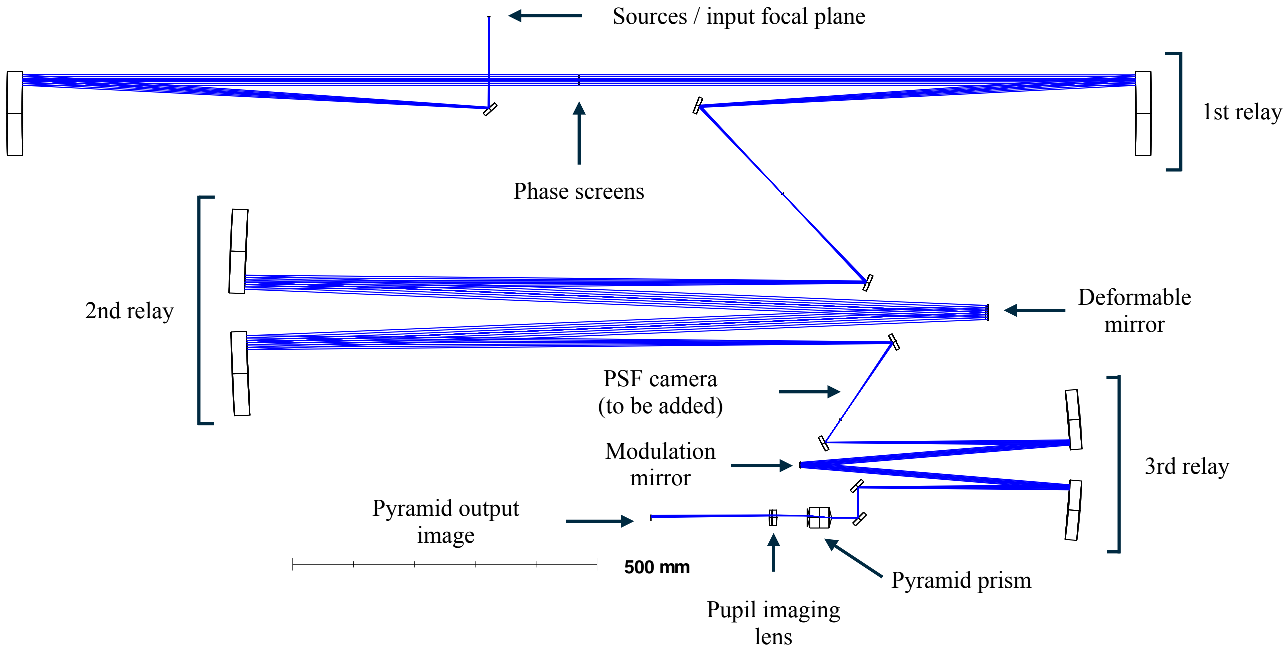


Figure 7: Zemax drawing of the bench from sources to the pyramid output

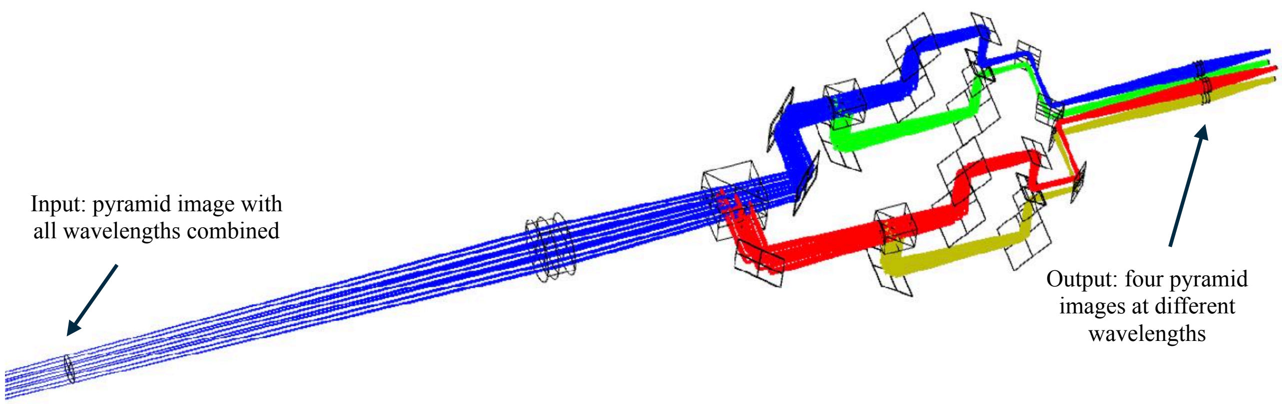


Figure 8: Zemax drawing of the colour splitter design. This design is preliminary and the exact focal lengths of the lenses and distances between the elements are being adjusted.

(17x17) device from ALPAO with 1.5mm actuator pitch. In between the second and third relay, a beam splitter allows the focal plane to be imaged on a visible CCD camera which is used to monitor the PSF. The third relay contains the Pyramid modulation mirror, at the output of which the modulated focal plane is imaged on the pyramid prism tip. The Pyramid follows the design approach of[15] that uses two back-to-back pyramidal prisms of different glass types (N-BAK4 and N-FK9) to control internal chromatic aberrations introduced by the prisms. After the pyramid prism, a lens images the PWFS pupils to obtain the final 4-pupil PWFS image. The optical design of the bench between the input focal plane and the first pyramid wavefront sensor image is shown in Figure 7. The bench represents a path length of 10 m due to the slow f\53 beam needed at the pyramid tip. necessary to account for the manufacturing tolerance pyramid vertex and separate the 4 pupils at the output of the pyramid prism.

The beam is then split onto two paths using a 50:50 beamsplitter. In the first path, an Offner relay re-images

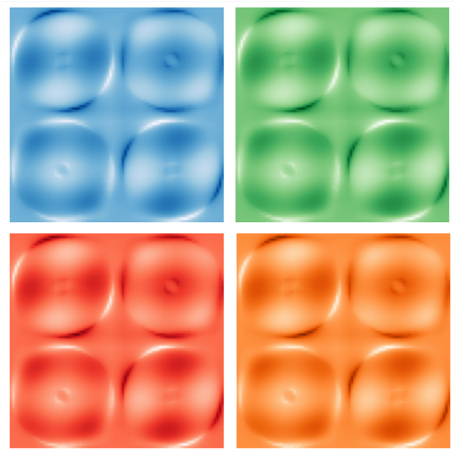

Figure 9: Illustration of the colour splitter output imaged on the CMOS camera

the pupil plane on the MKID array. The second path is made of a refractive relay, a series of beam splitters and a folding mirror, to separate the beam in four channels and bring them all to re-image $4 \times 4$ PWFS images on the CMOS camera, as illustrated in Figure 9. The preliminary layout of the colour splitter is shown in Figure 8. Equal intensity beam splitters create the four channels; the colour separation is made using filters situated before the last lens on each channel.

| Parameter | Value |
|---|---|
| Mirror actuator pitch | 20 cm |
| Number of actuators across the pupil | 15.5 |
| Telescope diameter | 3.1 m |
| Phase screen $r_0$ (at 500nm) | 16.1 cm |
| Number of subapertures across the pupil (MKID array) | 25 |
| Subaperture size (MKID array) | 12.4 cm |
| Maximum control speed (DM) | 1 kHz |

Table 2: Summary of the AO system characteristics when setting the mirror actuator pitch to represent 20 cm in the equivalent telescope aperture.

The dimensions of the AO system simulated on this bench have been selected to reproduce an XAO system . First, the ratio between actuator pitch and $r_0$ in the visible has been set to be close to one ($d_{act}/r_0 = 1.24$). In terms of equivalent dimensions on a telescope, if the actuator pitch corresponds to 20 cm (matching VLT/SPHERE AO system[16]) then the phase screen represents an $r_0$ of 16.1 cm at 500 nm, close to the median $r_0$ in Paranal of 15.7 cm.[17] We have the option to use two other phase screens representing lower $r_0$ of 14.6 cm and 10.6 cm. Second, both the ALPAO 292 actuator DM and CMOS detector (when using a readout window covering the $4 \times 4$ pupil images and binning the pixels) can run up to 1 kHz. The MKID pixel sampling rate can enable an AO-loop update rate faster than this as discussed in the next section. The system therefore provides XAO-resolution of sampling and correction albeit for a 3.1 meter diameter telescope, limited by the number of actuators on the DM. On the MKID array, the pupil images illuminate 25 pixels across the pupil - an oversampling factor of 1.6 - and the pupils are separated by 4 pixels. The dimensions of the pupil images on the CMOS camera are not yet fixed but at least as many pixels as on the MKID will be illuminated.

At the time of this proceeding the design of the bench is being finalised. The biggest outstanding decision regards the choice of the source for the bench. due to the slow f/53 input beam one difficulty resides in using a broadband source covering 400 nm to 1500 nm whilst providing a sufficiently small pinhole/fibre to create a diffraction-limited output at the vertex of the Pyramid. We are investigating the use of a filament or arc lamp coupled with a photonic crystal which provides an infinite single-mode propagation for the wavelength range of interest, or illuminating a pinhole of a sufficiently small size to keep a diffraction-limited source. In case these strategies do not provide a sufficient amount of light on the detectors, alternate options would be to combine the output of several superluminescent diodes into a single fibre or to use a supercontinuum white light laser.

### 4.2 MKID Camera

For the purposes of the initial demonstration, we intend to use a 1600 pixel MKID array. This array is currently being developed by SRON, based on hybrid NbTiN/Ta MKIDs,[18] and will likely consist of 4 feedlines. Each feedline will have 400 resonators (pixels) to limit the number of frequency "collisions", which leads to reduced pixel yield.[19] The entire array will be on a single chip, but the pixels addressed by a particular feedline will form a sub-array that will image a single sub-pupil of the output of the PWFS. The array will placed in our Bluefors SD dilution refrigerator and cooled to the operating temperature of around 60mK. It will be illuminated via an entrance window on the side of the cryostat, which will contain IR blocking filters to limit the thermal loading on the array.

The MKID readout system is a high-performance setup designed to efficiently process detected photon pulse data. The Radio-Frequency (RF) subsystem is a key component, providing a low-noise, broadband RF transceiver. This transceiver converts baseband signals to microwave to drive the MKID array and then back to the baseband. The ADC/DAC units interface the analog signals with the digital processing pipeline using an FPGA due to its high real-time processing capabilities (example of an existing MKID readout pipeline can be found in.[20]

The read-out system we are developing uses a Xilinx ZCU111 FPGA development board, with firmware developed by UCSB MazinLab.[21] This is combined with a custom RF interface board[22] to mix the signals to the 4-8GHz range required by the MKID resonators. In contrast to the previous MKID read-out systems, which typically use an FPGA for pulse detection and analysis, we will stream the phase data to a computer and use a GPU for this final stage. This approach leverages advanced computing resources for improved analysis, as well as easier development and maintenance. With a data sampling rate of 1MHz and 16-bit representation, the data rate can reach 4GB/s for 2000 detectors, requiring dual 25GbE links for real-time transfer. This setup, equipped with an Nvidia RTX A5000 GPU and an Nvidia network card, utilizes DPDK for direct memory transfers, ensuring the highest possible data rates.[23]

The pulse detection and analysis will be conducted in real-time on the GPU, with the phase stream from each resonator (pixel) processed in parallel. For the purposes of this demonstrator, we will use the standard approach of applying a matched filter and then triggering when the signal goes above a certain threshold. In this case, once the trigger time (photon arrival time) and the pulse height (photon energy) have been determined, this information will be delivered to the RTC. In the future, we will investigate more sophisticated pulse processing routines, including processing multiple photon events, observed during high photon fluxes. The flexibility of the GPU should enable us to flag these events and process them differently, overcoming an import limitation of existing, FPGA-based read-out architectures.

We will be using Durham Adaptive Optics (DAO) for the RTC system. Developed in-house for use in HARMONI, DAO is powerful enough for ELT scale instruments while remaining flexible enough to be used in the lab. DAO will be connected to the Readout computer via Ethernet network as well as the CMOS camera. The readout computer will have the option to stream either wavelength-binned time-integrated images built up from individual photon events over an artificial integration time or stream the individual photon events themselves at MHz rates. Using the colour-split images from the CMOS camera, DAO can correct the wavefront at different wavelengths. This can be reproduced by the MKID and readout computer using the binned images. We are investigating methods of using individual photons to optimise the wavefront correction.

### 4.3 Discussion

Assembly of the bench will begin before the MKID array is available. We will therefore first use the colour splitter combined with the CMOS camera to test the use of several wavebands to control the AO loop. With this setup, we will be able to develop the multi-wavelength calibration and control techniques methods, varying the number of wavebands we control and compare performance between any single waveband control and four-waveband polychromatic control. We will also look at the implementation of the OG tracking method described in Section

3.2. The CMOS camera will serve first as an element of reference to ensure that we are processing correctly the data coming out of the MKID array and later to compare the performance of the AO loop between the two sensors. Once the MKID array becomes available and is integrated within the bench, we plan to test the MKID energy sensitivity capabilities first. We will therefore investigate the impact of spectral resolution by looking at how many different wavebands can be controlled and how it affects the AO loop performance. Finally, we will explore the possibilities opened by the data stream format of the MKID read-out and conduct studies such as using frames of varying duration to ensure a constant SNR.

## 5. CONCLUSION

Initial AO performance simulations of a polychromatic PWFS using an MKID array and the development path towards an eventual on-sky demonstration have been presented here. The polychromatic PWFS involves developing a custom MKID array as the PWFS detector. The use of the MKID array provides several potential routes to improve PWFS performance in closed-loop through the ability of the MKID to discriminate between several narrow wavebands (typically of a several tens of nanometers over the VIS-NIR wavelength range). In this proceeding we have investigated the use of wavelength information to increase the observing passband and therefore to increase the number of photons detected whilst accounting for variations in the chromatic response of the PWFS, particularly for faint targets. Wavelength discrimination will also allow us to benefit from both the PWFS sensitivity of short wavelengths and the large dynamic range of long wavelengths. Simulations have shown this could result in 2 - 3 factor improvement in residual wavefront within the correction band.

To further demonstrate the MKID-PWFS concept and verify simulation results an optical bench is being built. At this point in time, the optical design has been completed. The design has been created to emulate the functionality of an XAO system for high-contrast imaging. The optical bench comprises a conventional PWFS configuration, whereby pupil images will be imaged onto two distinct detectors: initially a large-format CMOS detector and later the MKID array when it becomes available. A custom 4-colour beamsplitting and recombination system will be positioned between the CMOS and the PWFS prism. This will image the four pupil images in four wavebands between 400 - 900 nm using 40nm bandwidth interference filters, resulting in frames of $4 \times 4$ pupil images to verify the multi-waveband simulations in a situation where we have perfect knowledge of the wavelength. This will later be compared to the results obtained using the MKID array where MKID-specific effects such as saturation and colour confusion can be characterised. The AO loop is planned to run at 1 kHz, as we are implementing a full end-to-end real-time readout pipeline for the MKID array. The objective of this demonstrator is twofold: firstly, to demonstrate the proof of concept and secondly, to showcase initial improvements through the implementation of polychromatic wavefront reconstruction.

The demonstrator represents the initial phase of development for an XAO system for ELT-scale instrumentation. In order to achieve such a system, it is necessary to develop an MKID array that includes a greater number of pixels while maintaining the same level of performance. However, increasing the number of pixels per feedline can result in frequency "collisions", effectively lowering pixel yield across the array. Furthermore, there is potential for optimising the utilisation of pixels, whereby only those illuminated by the output of the pyramid are used.

## ACKNOWLEDGMENTS

This project has been funded by Science and Technology Facilities Council (STFC) grants (ST/S001409/1, ST/001360/1) and STFC's Centre for Instrumentation (CfI) program. The detector development at SRON is supported by the Netherlands Organisation for Scientific Research NWO (Vidi 213.149).

## REFERENCES

[1] Babcock, H. W., "The possibility of compensating astronomical seeing," *Publications of the Astronomical Society of the Pacific* **65**(386), 229–236 (1953).

[2] Kasper, M., Cerpa Urra, N., Pathak, P., Bonse, M., Nousiainen, J., Engler, B., Heritier, C. T., Kammerer, J., Leveratto, S., Rajani, C., Bristow, P., Le Louarn, M., Madec, P.-Y., Ströbele, S., Verinaud, C., Glauser, A., Quanz, S. P., Helin, T., Keller, C., Snik, F., Boccaletti, A., Chauvin, G., Mouillet, D., Kulcsár, C., and Raynaud, H.-F., "PCS — A Roadmap for Exoearth Imaging with the ELT," *Published in The Messenger vol. 182* **pp. 38-43**, 6 pages (2021).

[3] Ragazzoni, R., "Pupil plane wavefront sensing with an oscillating prism," *Journal of Modern Optics* **43**, 289–293 (Feb. 1996).

[4] Day, P. K., LeDuc, H. G., Mazin, B. A., Vayonakis, A., and Zmuidzinas, J., "A broadband superconducting detector suitable for use in large arrays," *Nature* **425**, 817–821 (Oct. 2003).

[5] Magniez, A., Bardou, L., Morris, T. J., and O'Brien, K., "MKID: an energy sensitive superconducting detector for the next generation of XAO systems," in [*Adaptive Optics Systems VIII*], Schmidt, D., Schreiber, L., and Vernet, E., eds., 94, SPIE, Montréal, Canada (Aug. 2022).

[6] de Visser, P. J., de Rooij, S. A., Murugesan, V., Thoen, D. J., and Baselmans, J. J., "Phonon-Trapping-Enhanced Energy Resolution in Superconducting Single-Photon Detectors," *Physical Review Applied* **16**, 034051 (Sept. 2021).

[7] Ragazzoni, R., Diolaiti, E., and Vernet, E., "A pyramid wavefront sensor with no dynamic modulation," *Optics Communications* **208**, 51–60 (July 2002).

[8] Chambouleyron, V., Fauvarque, O., Plantet, C., Sauvage, J.-F., Levraud, N., Cissé, M., Neichel, B., and Fusco, T., "Modeling noise propagation in Fourier-filtering wavefront sensing, fundamental limits and quantitative comparison," (Dec. 2022). arXiv:2212.13577 [astro-ph].

[9] Chambouleyron, V., Fauvarque, O., Janin-Potiron, P., Correia, C., Sauvage, J.-F., Schwartz, N., Neichel, B., and Fusco, T., "Pyramid wavefront sensor optical gains compensation using a convolutional model," *Astronomy & Astrophysics* **644**, A6 (Dec. 2020).

[10] Vidal, F., Gendron, E., Deo, V., Buey, J.-T. M., and Rousset, G., "A modal approach to optical gain compensation for the pyramid wavefront sensor," in [*Adaptive Optics Systems VI*], Schmidt, D., Schreiber, L., and Close, L. M., eds., 73, SPIE, Austin, United States (July 2018).

[11] Meeker, S. R., Mazin, B. A., Walter, A. B., Strader, P., Fruitwala, N., Bockstiegel, C., Szypryt, P., Ulbricht, G., Coiffard, G., Bumble, B., Cancelo, G., Zmuda, T., Treptow, K., Wilcer, N., Collura, G., Dodkins, R., Lipartito, I., Zobrist, N., Bottom, M., Shelton, J. C., Mawet, D., Eyken, J. C. v., Vasisht, G., and Serabyn, E., "DARKNESS: A Microwave Kinetic Inductance Detector Integral Field Spectrograph for High-contrast Astronomy," *Publications of the Astronomical Society of the Pacific* **130**, 065001 (Apr. 2018). Publisher: IOP Publishing.

[12] Walter, A. B., Fruitwala, N., Steiger, S., Bailey, J. I., Zobrist, N., Swimmer, N., Lipartito, I., Smith, J. P., Meeker, S. R., Bockstiegel, C., Coiffard, G., Dodkins, R., Szypryt, P., Davis, K. K., Daal, M., Bumble, B., Collura, G., Guyon, O., Lozi, J., Vievard, S., Jovanovic, N., Martinache, F., Currie, T., and Mazin, B. A., "The MKID Exoplanet Camera for Subaru SCExAO," *Publications of the Astronomical Society of the Pacific* **132**, 125005 (Nov. 2020).

[13] cheritier, "cheritier/OOPAO," (July 2024). original-date: 2021-05-07T10:04:50Z.

[14] Jocou, L., Rabou, P., Moulin, T., Magnard, Y., Hours, A., Pancher, F., Guieu, S., Carlotti, A., Delboulbé, A., Vérove, M., Stadler, E., Maurel, D., Rochat, S., Hénault, F., Dohlen, K., Thatte, N., Neichel, B., Vola, P., Clarke, F., Melotte, D., Tecza, M., and Schnetler, H., "HARMONI at ELT: development of the high-contrast module," in [*Adaptive Optics Systems VIII*], Schmidt, D., Schreiber, L., and Vernet, E., eds., 171, SPIE, Montréal, Canada (Aug. 2022).

[15] Tozzi, A., Stefanini, P., Pinna, E., and Esposito, S., "The double pyramid wavefront sensor for LBT," in [*Adaptive Optics Systems*], **7015**, 1454–1462, SPIE (July 2008).

[16] Sauvage, J.-F., Fusco, T., Petit, C., Costille, A., Mouillet, D., Beuzit, J.-L., Dohlen, K., Kasper, M., Suarez, M., Soenke, C., Baruffolo, A., Salasnich, B., Rochat, S., Fedrigo, E., Baudoz, P., Hugot, E., Sevin, A., Perret, D., Wildi, F., Downing, M., Feautrier, P., Puget, P., Vigan, A., O'Neal, J., Girard, J., Mawet, D., Schmid, H. M., and Roelfsema, R., "SAXO: the extreme adaptive optics system of SPHERE (I) system overview and global laboratory performance," *Journal of Astronomical Telescopes, Instruments, and Systems* **2**, 025003 (May 2016).

[17] Osborn, J. and Sarazin, M., "Atmospheric turbulence forecasting with a general circulation model for Cerro Paranal," *Monthly Notices of the Royal Astronomical Society* **480**, 1278–1299 (Oct. 2018).

[18] Kouwenhoven, K., Fan, D., Biancalani, E., De Rooij, S. A., Karim, T., Smith, C. S., Murugesan, V., Thoen, D. J., Baselmans, J. J., and De Visser, P. J., "Resolving Power of Visible-To-Near-Infrared Hybrid Ta / Nb Ti N Kinetic Inductance Detectors," *Physical Review Applied* **19**, 034007 (Mar. 2023).

[19] Szypryt, P., Meeker, S. R., Coiffard, G., Fruitwala, N., Bumble, B., Ulbricht, G., Walter, A. B., Daal, M., Bockstiegel, C., Collura, G., Zobrist, N., Lipartito, I., and Mazin, B. A., "Large-format platinum silicide microwave kinetic inductance detectors for optical to near-IR astronomy," *Optics Express* **25**, 25894–25909 (Oct. 2017). Publisher: Optica Publishing Group.

[20] McHugh, S., Mazin, B. A., Serfass, B., Meeker, S., O'Brien, K., Duan, R., Raffanti, R., and Werthimer, D., "A readout for large arrays of microwave kinetic inductance detectors," *Review of Scientific Instruments* **83**, 044702–044702 (Apr. 2012).

[21] Smith, J. P., Bailey, J. I., III, Cuda, A., Zobrist, N., and Mazin, B. A., "MKIDGen3: Energy-Resolving, Single-Photon-Counting MKID Readout on an RFSoC," (June 2024). arXiv:2406.09764 [astro-ph, physics:physics].

[22] Geng, D., O'Brien, K., Morris, T., Magniez, A., Hofmann, B., and Shaw, B. J., "MKIDS readout implementation with RFSOC," in [*X-Ray, Optical, and Infrared Detectors for Astronomy X*], **12191**, 1219110, SPIE (Aug. 2022).

[23] Geng, D., Barr, D., O'Brien, K., Magniez, A., Morris, T. J., Bardou, L., and Dimoudi, S., "Integrating FPGA and CPU/GPU technologies for enhanced MKIDs readout performance," in [*X-Ray, Optical, and Infrared Detectors for Astronomy XI*], SPIE.